Title	High performance germanium nanowire based lithium-ion battery anodes extending over 1000 cycles through in-situ formation of a continuous porous network
Authors	Kennedy, Tadhg;Mullane, Emma;Geany, Hugh;Osiak, Michal J.;O'Dwyer, Colm;Ryan, Kevin M.
Publication date	2014-01-13
Original Citation	Kennedy, T., Mullane, E., Geaney, H., Osiak, M., O'Dwyer, C. and Ryan, K. M. (2014) 'High-Performance Germanium Nanowire-Based Lithium-Ion Battery Anodes Extending over 1000 Cycles Through in Situ Formation of a Continuous Porous Network', Nano Letters, 14(2), pp. 716-723. doi: 10.1021/nl403979s
Type of publication	Article (peer-reviewed)
Link to publisher's version	http://pubs.acs.org/doi/abs/10.1021/nl403979s - 10.1021/nl403979s
Rights	© 2014 American Chemical Society. This document is the Accepted Manuscript version of a Published Work that appeared in final form in Nano Letters, copyright © American Chemical Society after peer review and technical editing by the publisher. To access the final edited and published work see https://pubs.acs.org/doi/abs/10.1021/nl403979s
Download date	2023-05-05 10:54:48
Item downloaded from	http://hdl.handle.net/10468/6113

High Performance Germanium Nanowire based Lithium-ion Battery Anodes Extending over 1000 Cycles Through In-situ Formation of a Continuous Porous Network

*Tadhg Kennedy [1], Emma Mullane [1], Hugh Geaney [2, 3], Michal Osiak [2, 3], Colm O'Dwyer [2, 3], Kevin M. Ryan [1]**

[1] Materials and Surface Science Institute and the Department of Chemical and Environmental Sciences, University of Limerick, Ireland

[2] Department of Chemistry, University College Cork, Cork, Ireland

[3] Tyndall National Institute, Lee Maltings, Cork, Ireland

ABSTRACT: Here we report the formation of high-performance and high-capacity lithium-ion battery anodes from high density germanium nanowire arrays grown directly from the current collector. The anodes retain capacities of ~ 900 mAh/g after 1100 cycles with excellent rate performance characteristics, even at very high discharge rates of 20-100C. We show by an ex-situ HRTEM and HRSEM study that this performance can be attributed to the complete restructuring of the nanowires that occurs within the first 100 cycles to form a continuous porous network that is mechanically robust. This restructured anode, once formed, retains a remarkably stable capacity with a drop of only 0.01% per cycle thereafter. As this

approach encompasses a low energy processing method where all the material is electrochemically active and binder free, the extended cycle life and rate performance characteristics demonstrated makes these anodes highly attractive for the most demanding lithium-ion applications such as long range battery electric vehicles.

KEYWORDS: Germanium nanowires, tin, lithium-ion battery, rate capability, network, porous

TEXT: Si and Ge nanowire (NW) based materials have emerged as viable candidates for next generation rechargeable lithium-ion battery anodes with energy and power densities that are multiples of current graphitic based electrodes.[1-7] The key advance is the capability of NWs to overcome the well-known pulverization problem that is detrimental to the cycle life and hence viability of their bulk counterparts.[8, 9] NWs also provide good electrical conductivity along their length, have a high interfacial area in contact with the electrolyte, have an optimal short diffusion distance for Li-ion transport and can be grown directly from current collectors, eliminating the need for binders and conductive additives. Ge (max. theoretical capacity of 1384 mAh/g) has received less attention than Si (3579 mAh/g), although it has a higher rate of diffusivity of Li at room temperature (400 ×) and a greater electrical conductivity (10,000 ×) making it suitable for high power applications.[10, 11] Gold is the most common catalyst for Ge NWs synthesis[4, 12-14], however as it is expensive and does not reversibly alloy with lithium[15], alternative more cost effective catalyst materials that can contribute to the specific capacity of the electrode are desirable.[16, 17]

Improving the cycle life of simple Ge NW arrangements as Li-ion anodes would be very interesting as their ease of processability and scalability, particularly if solution grown, can offer viable alternatives to graphitic materials. Reports to-date on binder-free Ge NW electrodes have only shown stability up to 50 cycles.[12, 13] A range of nanocomposite architectures have been employed that increase the stability of Ge based anodes over hundreds of cycles for example nanotube networks[18], dispersions of nanomaterials in active/inactive buffer matrices[19, 20], sheathing of nanostructures with carbon[21] and Ge NW-graphene composites[22-24]. A further interesting area of research is the incorporation of pores to improve the performance of Li-alloying nanostructures.[25-29] The advantages pertain to increased rate capability as charge transfer across the electrolyte/active material interface is facilitated by the large surface area. Furthermore, the void space provides room for the

expansion of the material during charging, alleviating the build-up of stress in the electrode. A recent in-situ TEM study by Liu et al. showed that Ge NWs form pores upon delithiation suggesting that a porous, nanostructured Ge architecture could be formed in-situ in the electrochemical cell through cycling.[30] However, this study is limited to a single NW and does not show the cumulative effect of cycling on a NW network over tens or hundreds of cycles.

Here we demonstrate stable cycling, over 1100 cycles, of Ge NWs grown directly from a current collector. We show by ex-situ high-resolution transmission electron microscopy (HRTEM) and high-resolution scanning electron microscopy (HRSEM) studies that the NW array transforms into a robust, porous network structure within the first 100 cycles. Once this network is formed it is highly stable, maintaining a capacity of ~ 900 mAh/g over the following 1000 cycles. The electrolyte additive, vinylene carbonate (VC), was found to play an important role, facilitating the formation of this stable network morphology. The electrode material described here has several advantages as it is formed in a low energy, wet-chemical process with Ge NWs nucleating and growing from an evaporated Sn layer on stainless steel. Sn also has a high maximum theoretical capacity (994 mAh/g), and we show both physically (HRTEM) and electrochemically (differential capacity plots) that the Sn seeds at the ends of the NWs reversibly alloy with lithium and contribute to the electrodes overall specific capacity. The NW electrode architecture performed exceptionally well in rate capability tests achieving a discharge capacity of 435 mAh/g after 80 cycles at a discharge rate of 100C. Considering the low cost and low energy required, especially when compared with CVD systems, we believe our synthetic protocol to be an attractive and scalable synthesis approach for high-performance group IV nanowire based electrodes.

A schematic of the modified reaction set up for the NW growth protocol in the solvent vapor growth (SVG) system[31, 32] is outlined in Figure 1a. A stainless steel substrate with an evaporated layer of Sn on its surface is placed in the vapor zone of a high boiling point solvent and diphenylgermane is injected into the flask at 430 ^{o}C. The Sn nanoparticle seeds form in-situ at this temperature and act as sinks for the Ge that decomposes from the precursor, facilitating high density NW growth by the vapor liquid solid (VLS) mechanism.

A typical SEM image of the as synthesized Ge NWs growing from the underlying current collector is shown in Figure 2a, with a higher resolution image of an individual NW with seed shown in Figure 2b. The NWs have a mean diameter of 73 nm with an average seed/NW diameter of 1.75:1, giving a 5:1 mass ratio of Ge:Sn in the resultant architecture. HRTEM of the Sn/Ge interface (Figure 2c) confirms that there is good contact between the seed and the NW. The FFT (Figure 2c, inset i) is indexed with spots that correspond to those expected for diamond cubic Ge and are consistent with a <111> growth direction. The FFT for the Sn catalyst (Figure 2c (inset ii)) is indexed with spots that correspond to tetragonal Sn. XRD analysis of the as synthesised NW array (Figure 2d) gave reflections consistent with cubic Ge (space group Fd-3m) and tetragonal Sn (space group I41/amd) with remaining peaks corresponding to the underlying stainless steel. Further characterization of the NWs was carried out using STEM and EDX techniques and is presented in the Supporting Information (Figure S2).

The electrochemical properties of the material were evaluated by galvanostatic cycling in a two electrode Swagelok cell cycled in the voltage range of 0.01V to 1.5V vs. Li/Li^{+} in a 1M $LiPF_6$ in EC/DMC (1:1 v/v) + 3wt% VC electrolyte. The electrodes had a loading density of 0.22 mg of active material per cm^2 and the average thickness of active material was between 1.5 – 2.0 μm. The as grown NWs on stainless steel were used directly as the working electrode and the material was cycled at a C/2 rate for 1100 cycles with the results shown in

Figure 3a and voltage profiles in Figure 3b. Importantly, the mass of both the Sn seed and the Ge NW were taken into account when calculating the gravimetric capacities, giving a maximum theoretical specific capacity for the composite anode of 1320 mAh/g. The NWs exhibited an initial discharge capacity of 1103 mAh/g and an average coulombic efficiency (C.E.) of 97.0%. Overall the electrode demonstrated extremely high performance, achieving a reversible capacity of 888 mAh/g after 1100 cycles, with the bulk of the fade occurring in the first 100 cycles. The stability of the capacity is notable considering the uncomplicated, binder free nature of the electrode.

The capacity loss beyond 100 cycles is minimal, dropping by only 0.01% per cycle. This suggest that the active material has formed a very stable structure, capable of withstanding the volume change without pulverization and without loss of contact from the current collector. To examine the structural changes occurring, ex-situ HRSEM analysis of electrodes was carried after 1, 10, 20 and 100 cycles (Figure 4 a-d). After 1 cycle (Figure 4a) the NW morphology is still distinguishable though there is some fusion between adjacent NWs and seeds (Supporting Information, Figure S4). This is most likely due to a phenomenon known as lithium assisted, electrochemical welding and has previously been reported for Si and Sn systems.[33, 34] After 10 cycles (Figure 4b) the overall wire-like form of the active material is retained; however there has been a significant texturing of the surface of the NWs through the formation of ridges and grooves. The deformation of the NWs after 20 cycles (Figure 4c) is much more severe, to the extent that the original NW form is all but lost. While the outline of some individual NWs can just be made out, on the whole the composition of the active material has fundamentally changed as the original, individual NWs have agglomerated and fused to form a network structure. Locally, the agglomeration of NWs with their neighbors leads to the emergence of interconnected island-like areas that form a network over the entire electrode (Supporting Information, Figure S5). After 100

cycles, the electrochemical restructuring of the active material is complete as all trace of the original NW morphology has been replaced by this network architecture (Figure 4d). The tilted SEM image illustrates that the active material remains well contacted to the current collector despite this restructuring process. The structure of this network was analyzed in more detail using HRTEM, with Figure 4e showing that the composition of the active material after 100 cycles is comprised of a porous, interconnected structure of interwoven Ge ligaments. The convoluted nature of the network is apparent with the higher magnification image in Figure 4f showing a mass of entangled Ge ligaments. The average ligament diameter is 5.6 nm ± 1.0 nm. Comparison of electrodes after 100 and 300 cycles (Supporting information, Figure S6 and S7) show that the charge-discharge process has little effect on the morphology of this porous network (Figure 1b) once it has formed. This is consistent with the capacity data (Figure 3a) and suggests that the ligaments have reached a critical size below which they resist any further deformation through cycling.

It was possible to isolate individual NWs through experiments with less dense growth (details in Supporting Information) to understand how this ligament structure evolves at the single NW level. After 1 cycle, ex-situ HRTEM and STEM images (Figure 5a,b) show that pores have formed throughout the NW, consistent with previous in-situ studies, as extraction of Li during dealloying produces vacancies that aggregate together into pores.[21, 30, 35, 36] The progression in deformation from 5-20 cycles is shown in HRTEM images and corresponding STEM images (Figure 5 c-h). The surface becomes progressively more textured due to the coalescence of small pores to form larger pores, having the effect of lowering the interfacial surface area between the NW and the electrolyte, thereby reducing the surface energy of the system. After 20 cycles, the NW structure has predominantly become a system of Ge ligaments with only the core containing concentrated areas of Ge. This compares well to the observation from dense NW growth as shown in Figure 4e-f where these Ge ligaments

combine and interweave with nearby neighbors to form the interconnected porous network of active material.

The direct effect of the electrolyte additive, vinylene carbonate, on the formation of this network and hence the electrochemical performance of the Sn seeded Ge NWs was investigated by comparing the capacity data of two electrodes cycled at a 1C rate in a VC containing (3wt. %) and a VC-free 1M $LiPF_6$ in EC/DMC electrolyte. The resulting capacities and C.E. values are plotted in Figure 6a. VC is a stable SEI former and is known to produce a more durable and cohesive SEI layer, preventing cracking and the constant re-exposing of the active material to the electrolyte with each cycle.[37-41] The results show that the VC containing electrolyte outperforms the VC-free electrolyte significantly (Figure 6a). 80.2% of the initial discharge capacity is retained after 200 cycles using the VC additive compared to only 57.8% for the standard electrolyte. There is a considerable improvement in the C.E. also with the VC containing electrolyte exhibiting a C.E. of 99.5% after 200 cycles compared to 96.3% for its VC-free equivalent. The poor performance of the VC-free electrode is due to the fact that the formation of the stable network of Ge ligaments does not occur without the presence of the additive. The VC-free NWs, like those cycled with VC, lose their wire like morphology completely and agglomerate together to form islands on the substrate, however these islands have a different structure to those formed with VC. The HRTEM images in Figure 6b and 6c show they no longer comprise of a network of interwoven Ge ligaments, but instead consist of a non-porous mass of amorphous Ge and Sn. In this form the islands readily lose contact with the current collector as evidenced by the low density of active material on the substrate in Figure 6d. The HRSEM image in Figure 6e illustrates this further as it shows the active material delaminating from the substrate at the edges of an island. Clearly, VC plays an important role in the high-performance of the electrode as it facilitates the formation of the more stable network of interconnected Ge

ligaments. On the whole, these results have demonstrated that the well-known problems of pulverisation, loss of contact with the current collector and an unstable SEI, which have limited the cycle life of Li-alloying anodes, can be overcome through an in-situ morphology transformation of the active material used in conjunction with SEI stabilizing electrolyte additives.

The rate capability of the Sn seeded Ge NWs was evaluated by charging and discharging the material for 5 cycles at rates of C/10, C/5, C/2, C, 2C and then back to C/10 (Figure 7a). The electrode exhibited discharge capacities at each rate of 1250, 1174, 1050, 821, 722 and 1188 mAh/g respectively. The high rate performance of the NWs was tested by charging and discharging at rates ranging from C/2 up to 60C (Figure 7b). The electrode performed very well up to rates of 10C maintaining a capacity of 538 mAh/g. Above rates of 10C however, the material performed poorly, exhibiting capacities of 202 mAh/g, 96 mAh/g and 58 mAh/g at rates of 20C, 40C and 60C respectively. The performance at higher rates is limited by the maximum achievable capacity during charging as previous studies have shown that germanium based electrodes can maintain high and stable capacities at very high discharge rates if the material is charged at a fixed, slower rate.[4, 10] In order to improve the discharge rate capability of the Sn seeded Ge NW electrode, the material was charged at a fixed rate of C/2 while discharging at very high current rates of up to 100C (Figure 7c). The NWs show minimal capacity fade up to discharge rates of 20C. At 20C a capacity of 1053 mAh/g was maintained which is 95% of the initial discharge capacity at the slower C/2 rate. At discharge rates of 60C and 100C, the electrode exhibited discharge capacities of 930 mAh/g and 354 mAh/g respectively. Notably, the electrode recovered 100% of its capacity when the current reverted to the initial C/2 rate. Figure 7d shows the capacity data where two different NW electrodes were charged at a 2C rate and discharged at either 20C or 100C. After 80 cycles the 20C rate electrode displayed a discharge capacity of 610 mAh/g, corresponding to a

92.6% capacity retention from the 1st cycle. Even at the very high rate of 100C, the NW electrode (435 mAh/g) outperforms the maximum achievable capacity at C rates for graphite based electrodes (372 mAh/g). To the best of our knowledge, there is no literature report of conventional graphite materials that can sustain a workable capacity at 20 C, demonstrating the high performance capability of these porous Ge network architectures.

To investigate the electrochemical processes occurring during charging and discharging, the differential capacity of the first two cycles of an electrode charged and discharged at a C/5 rate was plotted with the corresponding voltage profiles (Figure 8a). As a means of distinguishing between the peaks corresponding to the lithiation/delithiation of Ge and Sn respectively, the differential capacity plot (DCP) for a Sn only electrode is overlaid on that for the Sn seeded Ge NW electrode. Apart from the broad peak that only occurs between 1050 mV and 850 mV in the first cycle due to SEI formation, each subsequent peak represents a phase change associated with the alloying and dealloying reactions of Li with the active material (full analysis of each peak in Supporting Information). A sharp peak at 350 mV, associated with the alloying of Li with crystalline Ge (c-Ge), occurs in the first cycle and is replaced by a broader peak at 370 mV in the second cycle as a result of the amorphization of the NW. Sharp peaks are indicative of a transformation from a crystalline phase to an amorphous phase. The DCP's clearly illustrate the dual cycling of both the Ge NW and the Sn seed. The electrochemical response due to the phase transitions of Ge and Sn during the 1st and 2nd cycles differ only in the charge section of the curves, whereas the discharge curves are almost identical, suggesting a common mechanism exists for dealloying. This is due to the fact that the initial morphology of the material is different, with crystalline Ge and Sn giving a different electrochemical response to amorphous Ge and Sn. Consequently, it is expected that the phase transitions occurring during the delithiation process should also be affected by the morphology of the lithiated alloy, with delithiation of c-$Li_{15}Ge_4$ expected to

give a different electrochemical response to delithiation of a-$Li_{15}Ge_4$. This is confirmed when a Sn seeded Ge NW electrode is charged to a potential of 125 mV, just above the crystallization potential of $Li_{15}Ge_4$. Comparison of the differential capacities (Figure 8b) shows dealloying of a-$Li_{15}Ge_4$ (a-$Li_{15}Ge_4$ → a-Li_xGe; $0 < x < 3.75$) occurs at a much lower potential of 235 mV compared to 460 mV for c-$Li_{15}Ge_4$ (c-$Li_{15}Ge_4$ → a-$Li_{15}Ge_4$ → a-Li_xGe; $0 < x < 3.75$). Delithiation above potentials of 570 mV induces an identical electrochemical response in both curves indicating that the dealloying mechanism is the same in this potential range.

In summary, Sn seeded Ge NWs were successfully grown from stainless steel current collectors through a low cost, SVG system. When used as an anode material for Li-ion batteries, the NW electrodes exhibited excellent capacity retention over 1100 cycles at a C/2 rate. Our investigations of the effect of cycling on the morphology of the NWs revealed that they undergo a complete restructuring to form a porous network of interconnected Ge ligaments that is fundamental to the capacity retention of the electrode. Stabilization of the SEI layer through addition of the electrolyte additive VC was also found to be crucial in obtaining a high performing electrode as it facilitates the formation of the network. Voltage profiles and differential capacity plots revealed that the NWs behave as a composite anode material as both the Ge NWs and the Sn seed reversibly alloy with Li. We believe that the fabrication of Sn seeded Ge NW electrodes via the SVG system is a scalable method and their application as anodes for Li-ion batteries offers a viable alternative to conventional graphite electrodes, as they exhibit comparable stability and higher capacities over extended cycles. Furthermore the excellent high-rate capabilities while discharging suggest that the NWs may also be suited for high power applications that require very high discharge rates such as battery electric vehicles and power tools.

FIGURES

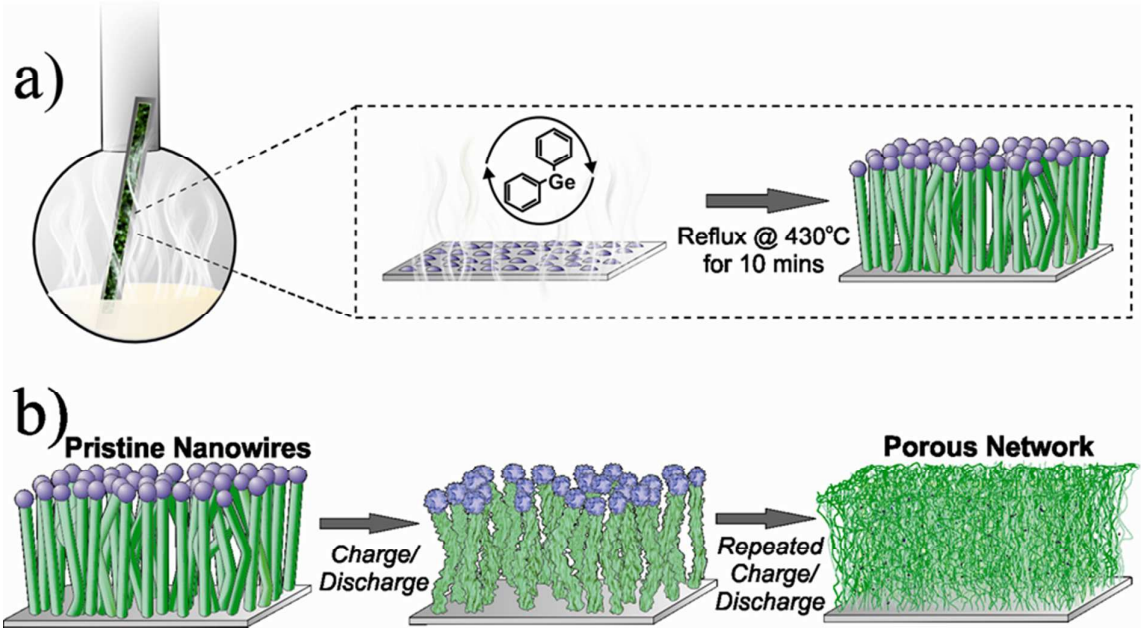

Figure 1: (a) Schematic illustrating the synthetic method used for NW growth. A pre-treated stainless steel substrate is placed in the vapor phase of a high boiling point solvent via a simple glassware based set-up. The temperature of the flask is ramped to 430^{o}C before injection of the germanium based precursor. Growth proceeds via the well-known VLS mechanism. (b) Schematic showing the cumulative effect of cycling on the NW architecture. The pristine Ge NW array is transformed into a porous, interconnected network of active material as a consequence of the charge/discharge process. The transformation occurs over the first 100 cycles.

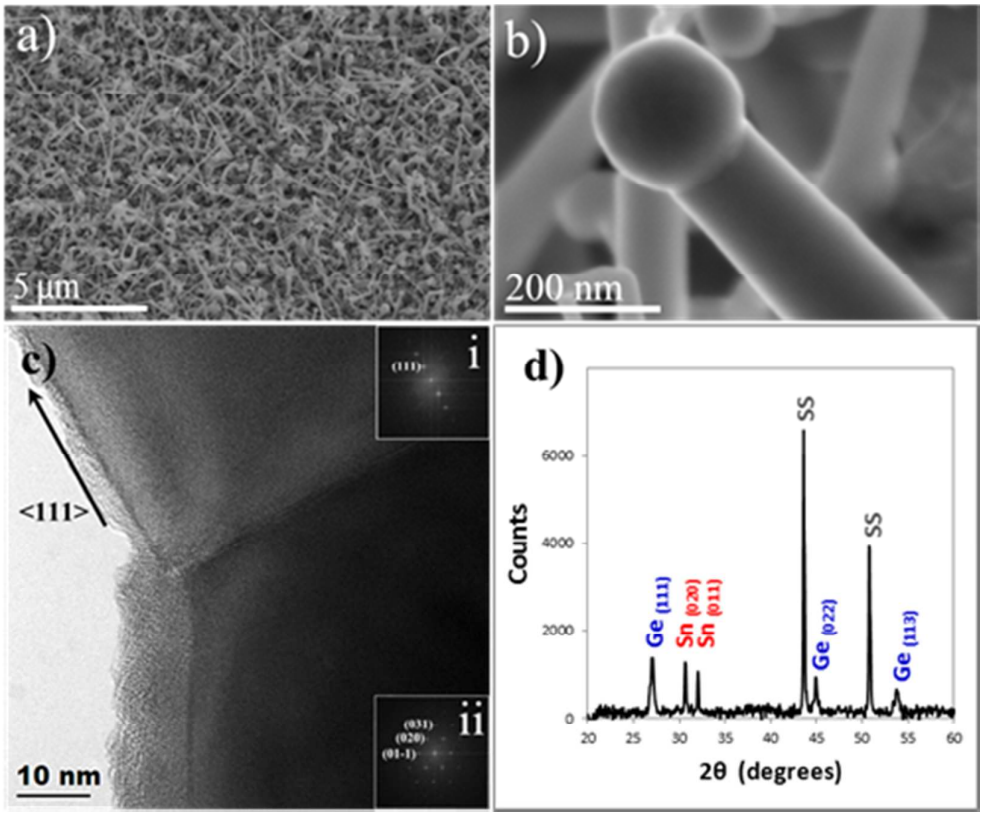

Figure 2: a) HRSEM image showing the Sn seeded Ge NWs growing from the stainless steel substrate in high density. b) High magnification HRSEM image of a Ge NW. A spherical Sn seed is clearly visible at the end of the NW. c) HRTEM image of the Sn/Ge interface of a NW with inset FFTs indexed for cubic Ge (i) and tetragonal Sn (ii) respectively. d) XRD results of the Sn seeded Ge NWs showing reflections corresponding to cubic Ge, tetragonal Sn and the SS current collector.

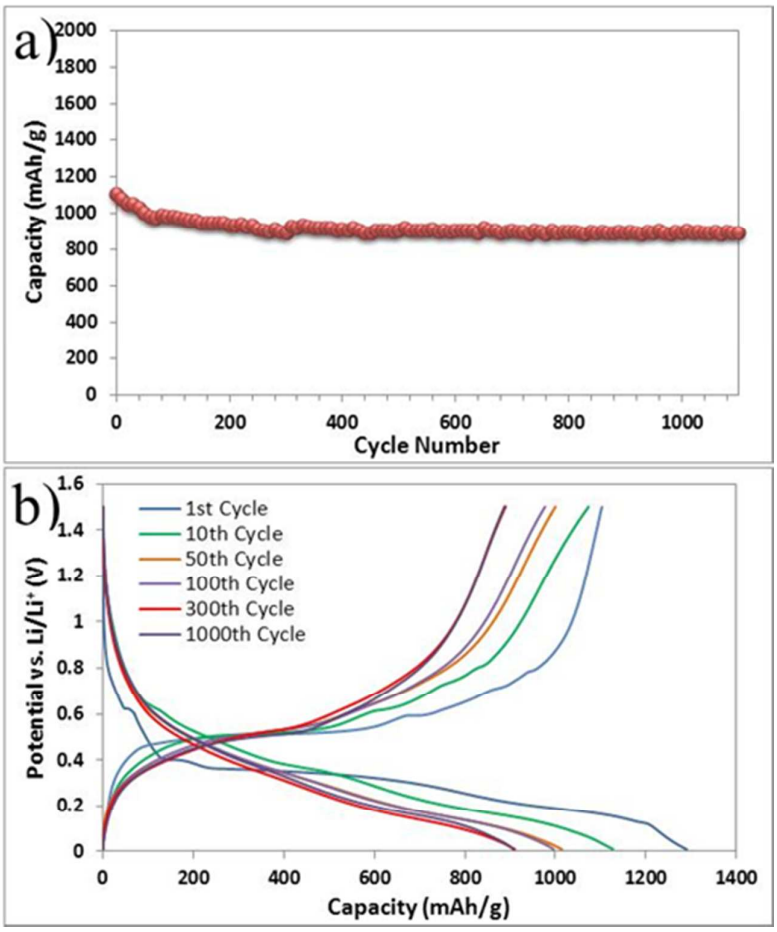

Figure 3: a) Discharge capacities of the Sn seeded Ge NW electrode over 1100 cycles. The active material was charged and discharged at a C/2 rate in the potential range of 0.01 – 1.5 V. b) Voltage profiles of 1st, 10th, 50th, 100th, 300th and 1000th cycle of the electrode cycled in a). The profiles show characteristic plateaus corresponding to the lithiation and delithiation of both Ge and Sn.

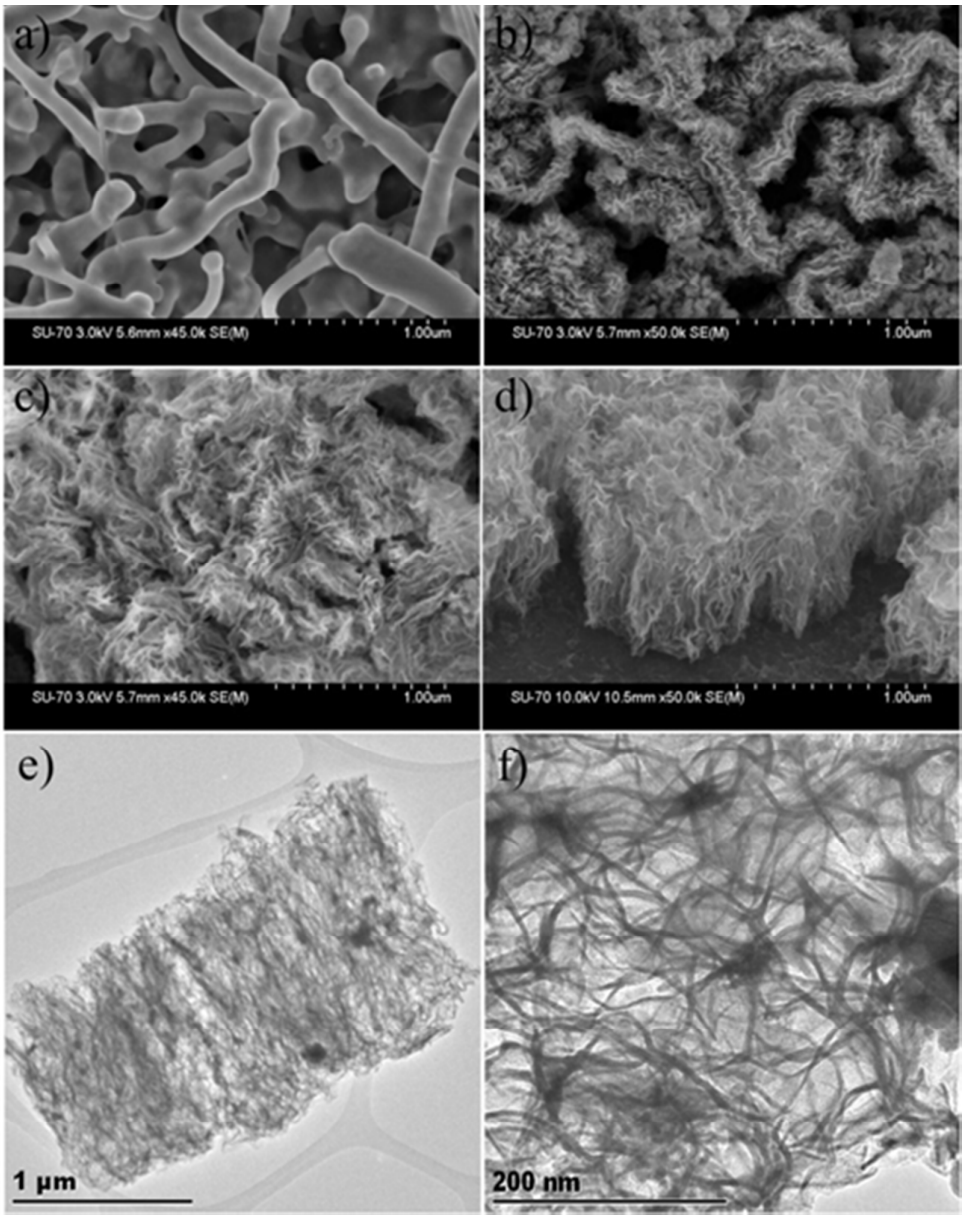

Figure 4: a-d) SEM images of Sn seeded Ge NWs after 1, 10, 20 and 100 cycles respectively: a) After 1 cycle the NWs retain a relatively smooth surface. Some evidence of fusion between adjacent NWs is present b) After 10 cycles the surface of the NWs has become much more textured with the presence of grooves and ridges evident c) After 20 cycles individual NWs are harder to identify as the extent of fusion between neighbouring NWs has increased significantly d) After 100 cycles the original NW morphology is lost having been replaced by a network of interconnected active material e) Low magnification

TEM image of the network architecture formed after 100 cycles; f) High magnification TEM image network formed after 100 cycles. The convoluted nature of the interconnected Ge ligaments is apparent.

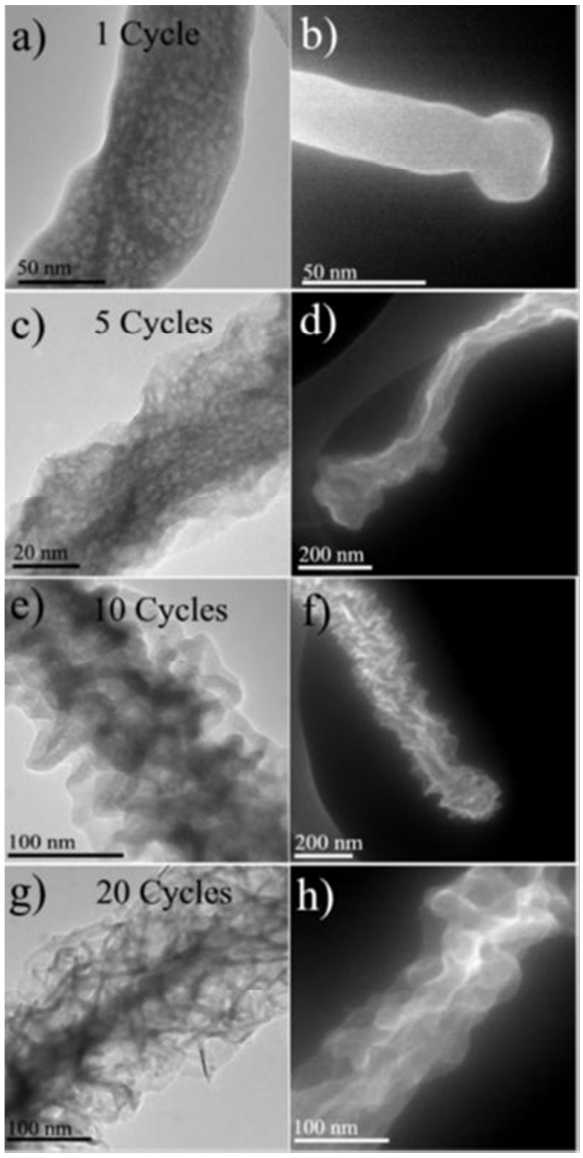

Figure 5: TEM and STEM images showing the effect of the alloying and dealloying processes on the structural integrity of the NWs. Images are shown of the NWs after a,b) 1 Cycle: Small pores have formed throughout the NW. The surface of the NWs remains smooth.; c,d) 5 Cycles: The effect of cycling has roughened the surface of the NWs; e,f) 10 Cycles: Ridges and grooves have formed on the NWs through the agglomeration of pores at the surface; g,h) 20 cycles: Further agglomeration of smaller pores to form larger pores has occurred resulting in the formation of ligaments of active material in all but the core of the NW.

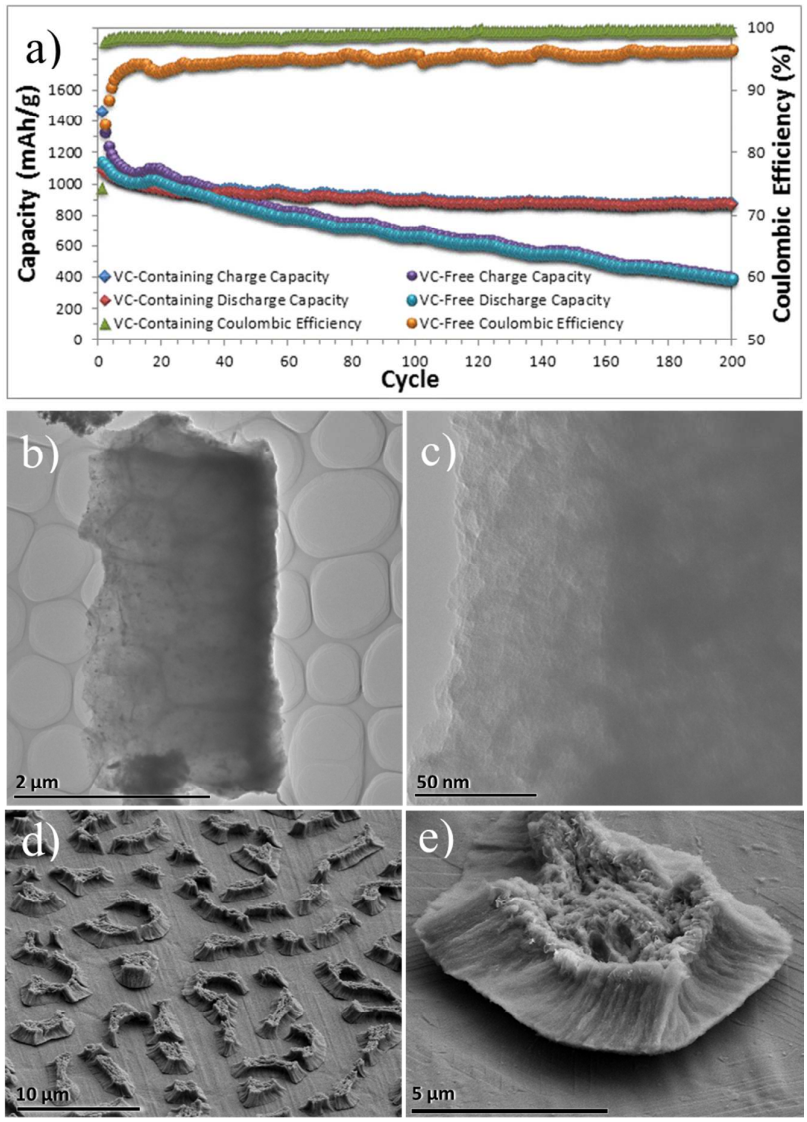

Figure 6: a) Comparison of the capacity data and C.E. values of two Sn seeded Ge NW electrodes using two electrolytes, one with VC (1M LiPF6 in EC/DMC + 3wt% VC) and one without VC (1M LiPF6 in EC/DMC). The electrodes were cycled at a C rate in the voltage range of 0.01 – 1.5 V. The VC containing electrolyte outperforms its VC-free equivalent as the SEI former facilitates the formation of the stable, porous network of Ge ligaments; b,c) Low and high magnification TEM images of the active material after 100 cycles using the VC-free electrolyte. The active material has formed a non-porous mass of Ge and Sn quite

different to the network of Ge ligaments formed with the VC containing electrolyte; d) Low magnification SEM image of the islands of active material on the substrate after 100 cycles using the VC-free electrolyte. The low density of active material indicates that the material readily loses contact with the current collector, explaining the poor performance of the electrode. e) SEM image of an island of active material after 100 cycles using the VC-free electrolyte. The active material is clearly delaminating from the current collector.

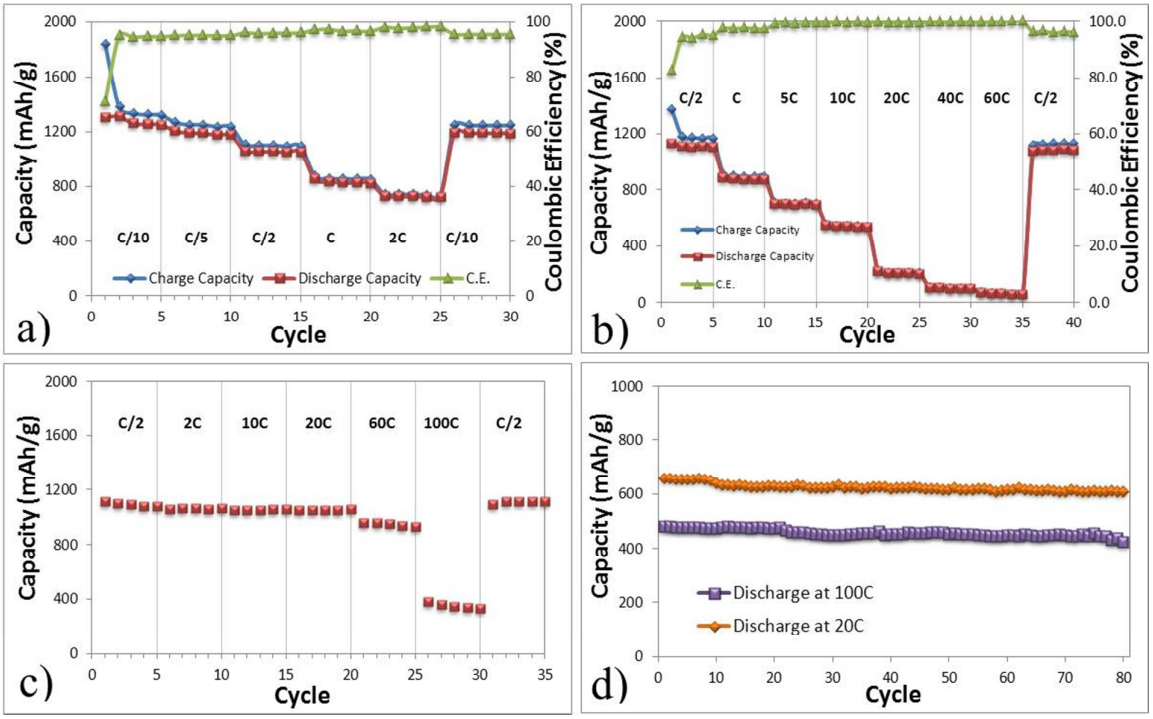

Figure 7: Rate capability, high rate capability and high discharge rate performance of the Sn seeded Ge NW electrodes cycled in the voltage range of 0.01 – 1.5 V a) The charge and discharge capacities and the C.E. values are shown at 5 different rates from C/10 up to 2C and then back to C/10 b) The high rate capability of the electrodes is shown. The capacities and the C.E. values of an electrode charged and discharged at rates of C/2, C, 5C, 10C, 20C, 40C, 60C and then back to C/2 is presented. c) The discharge capacities measured for 5 cycles at 6 different discharge rates are shown. The charge rate was kept constant at C/2 for all cycles. d) Capacity data showing discharge capacities of the material at 20C and 100C discharge rates. The electrodes were charged at a constant rate of 2C.

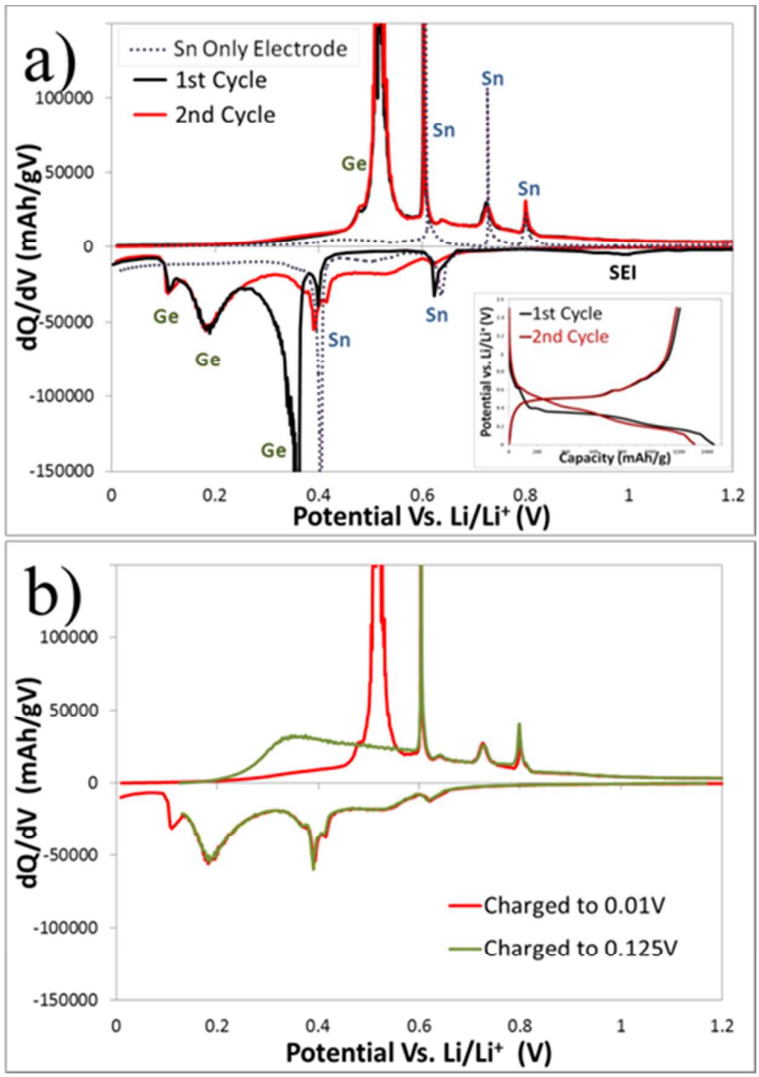

Figure 8: a) Differential capacity plot of the 1st and 2nd cycle of a Sn seeded Ge NW electrode and an electrode composed of a 20 nm layer of Sn evaporated onto a SS current collector. The electrodes were cycled at a C/5 rate in the potential range of 0.01 – 1.5V. The corresponding voltage profiles are inset. b) Differential capacity plot of a Sn seeded Ge NW electrode fully charged to 0.01V and then subsequently charged to 0.125V.

ASSOCIATED CONTENT

Additional experimental details, experimental data, electron microscopy images of cycled NWs, XRD of cycled NWs, size distribution of NWs before and after charging, differential capacity plots. This material is available free of charge via the Internet at http://pubs.acs.org.

AUTHOR INFORMATION

Corresponding Author

E-mail: Kevin.M.Ryan@ul.ie

Notes

The authors declare no competing financial interest.

ACKNOWLEDGMENT

This work was supported by Science Foundation Ireland (SFI) under the Principal Investigator Program under Contract No.. 11PI-1148 and also by EU FP7 funding - GREENLION Project - Contract nº 285268. T.K. acknowledges Intel Ireland and IRCSET for funding.

REFERENCES

1. Chan, C. K.; Peng, H.; Liu, G.; McIlwrath, K.; Zhang, X. F.; Huggins, R. A.; Cui, Y. *Nat. Nanotechnol.* **2007,** *3*, 31-35.
2. Chockla, A. M.; Harris, J. T.; Akhavan, V. A.; Bogart, T. D.; Holmberg, V. C.; Steinhagen, C.; Mullins, C. B.; Stevenson, K. J.; Korgel, B. A. *J. Am. Chem. Soc.* **2011***, 133*, 20914-20921.
3. Chockla, A. M.; Klavetter, K.; Mullins, C. B.; Korgel, B. A., *Chem. Mater.* **2012,** 24, 3738-3745.
4. Chockla, A. M.; Klavetter, K.; Mullins, C. B.; Korgel, B. A. *ACS Appl. Mater. & Interfaces* **2012**, 4, 4658-4664.
5. Geaney, H.; Kennedy, T.; Dickinson, C.; Mullane, E.; Singh, A.; Laffir, F.; Ryan, K. M. *Chem. Mater.* **2012,** *24*, 2204-2210.
6. Kim, H.; Cho, J. *Nano Lett.* **2008,** *8*, 3688-3691.
7. Yuan, F.-W.; Yang, H.-J.; Tuan, H.-Y. *ACS Nano* **2012***, 6*, 9932-9942.
8. Choi, N. S.; Yao, Y.; Cui, Y.; Cho, J. *J. Mater. Chem.* **2011**, *21*, 9825-9840.
9. Wu, H.; Cui, Y. *Nano Today* **2012**, *7,* 414-429.
10. Graetz, J.; Ahn, C.; Yazami, R.; Fultz, B. *J. Electrochem.* Soc. **2004,** *151*, A698-A702.
11. Wang, D.; Chang, Y. L.; Wang, Q.; Cao, J.; Farmer, D. B.; Gordon, R. G.; Dai, H. *J. Am. Chem. Soc.* **2004,** *126*, 11602-11611.
12. Chan, C. K.; Zhang, X. F.; Cui, Y., *Nano Lett.* **2008,** *8*, 307-309.
13. Ko, Y. D.; Kang, J. G.; Lee, G. H.; Park, J. G.; Park, K. S.; Jin, Y. H.; Kim, D. W. *Nanoscale* **2011**, *3*, 3371-3375.
14. Tan, L. P.; Lu, Z.; Tan, H. T.; Zhu, J.; Rui, X.; Yan, Q.; Hng, H. H. *J. Power Sources* **2012**, *206*, 253-258.
15. Chockla, A. M.; Bogart, T. D.; Hessel, C. M.; Klavetter, K.; Mullins, C. B.; Korgel, B. A. *J. Phys. Chem. C* **2012**, *116*, 18079-18086.
16. Geaney, H.; Dickinson, C.; Barrett, C. A.; Ryan, K. M. *Chem. Mater.* **2011,** *23*, 4838-4843.
17. Mullane, E.; Geaney, H.; Ryan, K. M. *Chem. Commun.* **2012,** *48*, 5446-5448.
18. Park, M. H.; Cho, Y.; Kim, K.; Kim, J.; Liu, M.; Cho, J. *Angew. Chem.* **2011**, *123*, 9821-9824.
19. Cui, G.; Gu, L.; Zhi, L.; Kaskhedikar, N.; van Aken, P. A.; Müllen, K.; Maier, J. *Adv. Mater.* **2008,** *20*, 3079-3083.
20. Yu, Y.; Yan, C.; Gu, L.; Lang, X.; Tang, K.; Zhang, L.; Hou, Y.; Wang, Z.; Chen, M. W.; Schmidt, O. G. *Adv. Energy Mater.* **2013**, *3*, 281-285.
21. Seo, M. H.; Park, M.; Lee, K. T.; Kim, K.; Kim, J.; Cho, J. *Energy Environ. Sci.* **2011,** *4*, 425-428.
22. Chockla, A. M.; Panthani, M. G.; Holmberg, V. C.; Hessel, C. M.; Reid, D. K.; Bogart, T. D.; Harris, J. T.; Mullins, C. B.; Korgel, B. A. *J. Phys. Chem. C* **2012**, *116*, 11917-11923.
23. Ren, J.-G.; Wu, Q.-H.; Tang, H.; Hong, G.; Zhang, W.; Lee, S.-T. *J. Mater. Chem. A* **2013**, *1*, 1821-1826.
24. Xue, D. J.; Xin, S.; Yan, Y.; Jiang, K. C.; Yin, Y. X.; Guo, Y. G.; Wan, L. J. *J. Am. Chem. Soc.* **2012**, *134*, 2512-2515.
25. Vu, A.; Qian, Y.; Stein, A. *Adv. Energy Mater.* **2012,** *2*, 1056-1085.
26. Song, T.; Jeon, Y.; Samal, M.; Han, H.; Park, H.; Ha, J.; Yi, D.K.; Choi, J.M.; Chang, H.; Choi, Y.M.; Paik, U. *Energy Environ. Sci.* **2012,** *5*, 9028-9033.

27. Yang, L.; Gao, Q.; Li, L.; Tang, Y.; Wu, Y. *Electrochem. Commun.* **2010,** *12*, 418-421.
28. Liu, X.; Zhao, J.; Hao, J.; Su, B. L.; Li, Y. *J. Mater. Chem. A* **2013**, *1*, 15076-15081.
29. Park, M.-H.; Kim, K.; Kim, J.; Cho, J. *Adv. Mater.* **2010,** *22*, 415-418.
30. Liu, X. H.; Huang, S.; Picraux, S. T.; Li, J.; Zhu, T.; Huang, J. Y. *Nano Lett.* **2011,** *11*, 3991-3997.
31. Mullane, E.; Kennedy, T.; Geaney, H.; Dickinson, C.; Ryan, K. M. *Chem. Mater.* **2013**, *25*, 1816-1822
32. Geaney, H.; Gunning, R. D.; Laffir, F. R.; Ryan, K. M. *Chem. Commun.* **2011,** *47*, 3843-3845.
33. Courtney, I. A.; McKinnon, W. R.; Dahn, J. R. *J. Electrochem.* Soc. **1999,** *146*, 59-68.
34. Karki, K.; Epstein, E.; Cho, J.-H.; Jia, Z.; Li, T.; Picraux, S. T.; Wang, C.; Cumings, J. *Nano Lett.* **2012**, *12*, 1392-1397.
35. Sieradzki, K.; Erlebacher, J.; Karma, A.; Dimitrov, N.; Aziz, M. *Nature* **2001,** *410*, 450-453.
36. Chen, Q.; Sieradzki, K. *Nature Mater.* **2013**, DOI: 10.1038/nmat3741
37. Wu, H.; Chan, G.; Choi, J. W.; Ryu, I.; Yao, Y.; McDowell, M. T.; Lee, S. W.; Jackson, A.; Yang, Y.; Hu, L. *Nat. Nanotechnol.* **2012**, *7*, 310-315.
38. Ulldemolins, M.; Le Cras, F.; Pecquenard, B.; Phan, V. P.; Martin, L.; Martinez, H. *J. Power Sources* **2012,** *206*, 245-252.
39. El Ouatani, L.; Dedryvere, R.; Siret, C.; Biensan, P.; Reynaud, S.; Iratcabal, P.; Gonbeau, D. *J. Electrochem. Soc.* **2009**, *156*, A103-A113.
40. Aurbach, D.; Gamolsky, K.; Markovsky, B.; Gofer, Y.; Schmidt, M.; Heider, U. *Electrochim. Acta.* **2002**, *47*, 1423-1439.
41. Chen, L.; Wang, K.; Xie, X.; Xie, J. *J. Power Sources* **2007**, 174, 538-543.

TOC: